Double Layered CeO2-Co3O4-CuO Based Anode for Direct Utilisation of Methane or Ethanol in SOFC

Sarruf, Bernardo; Hong, Jong-Eun; Steinberger-Wilckens, Robert; Miranda, Paulo Emilio

DOI:
10.1149/07801.1343ecst

Document Version
Peer reviewed version

Double Layered CeO_2-Co_3O_4-CuO Based Anode for Direct Utilisation of Methane or Ethanol in SOFC

B. J. M. Sarruf[a], J. –E. Hong[b,c], R. Steinberger-Wilckens[b], P. E. V. Miranda[a]

[a] Hydrogen Laboratory/COPPE, Metallurgical and Materials Engineering, Federal University of Rio de Janeiro - 21942-971 Rio de Janeiro, RJ, Brazil
[b] Centre for Fuel Cell and Hydrogen Research - School of Chemical Engineering, University of Birmingham Edgbaston, Birmingham, West Midlands B15 2TT, UK
[c] Fuel Cell Laboratory, New and Renewable Energy Research Division – Korea Institute of Energy Research 152, Gajeong-ro, Yuseong-gu, Daejeon 34129, South Korea

The present work aims at producing an electrocatalyst suitable to be used as anode in solid oxide fuel cells that operate with hydrocarbons or alcohols as fuel. The main challenge is to avoid carbon deposition during operation with carbonaceous fuels. Therefore, a cerium-cobalt-copper anode was developed, characterised and tested with methane or ethanol fuel, resulting in reasonable power densities and no evidence of carbon deposition as confirmed by Raman spectroscopy. SEM/EDX analysis showed the integrity of anode microstructure and phase distribution after the ageing procedure.

Introduction

Reforming of hydrocarbons is a process widely used in industry to convert (predominately) natural gas into syngas for subsequent further hydrogen production or purification, or as a chemical raw product. Techniques such as steam and dry reforming, shown in Equations 1 and 2, respectively, are applied for methane conversion into hydrogen and Carbon Monoxide by using a nickel or copper catalyst (1).

$$CH_4 + H_2O = CO + 3H_2, \quad \Delta H = +206\ kJmol^{-1} \qquad [1]$$

$$CH_4 + CO_2 = 2CO + 2H_2, \quad \Delta H = -41\ kJmol^{-1} \qquad [2]$$

The catalytic partial oxidation is another reaction path for the oxidation of methane which produces hydrogen and carbon monoxide – if partial oxidation may occur – as well as carbon dioxide when total oxidation takes place. However, the methane oxidation can be promoted by an electrochemical oxidation with O^{2-} ions. Equations 3 and 4 show the reaction processes of partial and total electrochemical oxidation, respectively (2).

$$CH_4 + O^{2-} = CO + 2H_2 + 2e^-, \quad \Delta H = +206\ kJmol^{-1} \qquad [3]$$

$$CH_4 + 4O^{2-} = CO_2 + 2H_2O + 8e^-, \quad \Delta H = -41\ kJmol^{-1} \qquad [4]$$

Furthermore, nickel-based anodes have shown to work as state-of-the-art, when hydrogen is fed as fuel, and even for hydrocarbon fuels. However, nickel-based anodes promote coking, which covers the catalyst and thus de-activates it, and in addition clogs the anode pore microstructure and the fuel tubings (3).

Ceria-based anodes, especially those with copper addition in its composition, have been shown to have interesting results for the use with hydrocarbon and alcohol fuels directly converted in SOFCs. Cerium oxide, as a mixed ionic electronic conductor (MIEC), has shown to be a suitable material for the catalytic oxidation of hydrocarbon fuels whereas copper presents the ability of avoiding coking over the catalyst surface and increasing electronic conductivity of the anode (4).

Therefore, the aim of this work was to develop a suitable ceria-copper electrocatalyst to serve as anode in SOFCs. The material was mainly composed by a CeO_2 matrix mixed with cobalt and copper oxides.

Materials and Methods

Firstly, two bimetallic ceria-based electrocatalyst materials were synthesised by the amorphous citrate method. The former composition with a molar proportion of Ce:Co:Cu – 2:1:1, and the latter with a proportion 1:2:1. The details of the citrate synthesis procedure are described in (5).

The two different powders were characterised by X-ray diffraction (XRD) using a Bruker D8 diffractometer ranging from 10˚ to 90˚ of 2θ varying each 0.02˚ with a monochromatic Cu K_α = 0.15418 nm radiation source. XRD analysis was done on the as-synthesised powder and after annealing it at 800 ˚C during two hours. Rietveld refinement was applied to the X-ray raw data using the FullProf Suite® software in which the background was described by a linear interpolation of pre-determined points with refinable heights.

Temperature-programmed reduction – TPR – was performed on the powders after the annealing treatment to test the reducibility of each compound. A Quantachrome ChemBET Pulsar TPR/TPD unit was used for this with approximately 20 mg of powder in a quartz reactor that ranged from room temperature to 900 ˚C in 5 ˚C min^{-1} steps. The reducing gas mixture consisted of 5% hydrogen in balanced nitrogen.

The powders were pelletised and then sintered to be submitted to a DC 4-probe conductivity test that was measured from 650˚C to 850˚C. Pellets were pressed in a uniaxial press die with 20 mm diameter at 2.5 tons of force and then sintered at 1000˚C to achieve densification.

After powder characterisation, single cells were assembled using a scandia/ceria-doped zirconia electrolyte support of Fuel Cell Materials onto which a lanthanum strontium-doped manganite (LSM) cathode was screen printed and sintered at 1100˚C for two hours. For the anode, an inner layer composed of a mixture of CeO_2 and ScCeSZ was applied between the electrolyte and the anode material aiming to decrease thermal incompatibilities. After the inner layer was printed and sintered at 1300˚C for three hours,

the first layer of the anode (Ce:Co:Cu – 2:1:1) was deposited by screen printing over the inner layer and dried at 150˚C for 30 minutes. After that, the last layer of the anode (Ce:Co:Cu – 1:2:1) was screen printed and the ensemble was calcined at 900˚C for two hours.

Electrochemical tests consisting of I-V curves were performed whilst the cathode was fed with pure oxygen as oxidant and the anode with hydrogen, methane, or ethanol as fuels. Tests were performed on two cells and ran on two different test rigs; the former at the University of Birmingham, and the latter at the Federal University of Rio de Janeiro to attest for reproducibility. *Post-mortem* analysis was carried out to assess carbon deposition on the anode by using Raman spectroscopy with a 633 nm wavelength laser in a Renishaw inVia Raman microscope. Samples were scanned from 3200 to 100 cm^{-1} with an acquisition time of 20 seconds and 1% of the laser total power. In addition, SEM/EDX analysis was performed on a sample of an anode that was reduced and aged for 50 hours at 800˚C in a hydrogen-rich atmosphere.

Results and Discussion

Figure 1 shows the spectra for the synthesised powders. The red dashed lines represent the spectra of the powders as-synthesised whilst the continuous black line is the spectrum for each powder after heat treatment at 800˚C. It can be observed that for both powders the peaks become narrower and sharper after heat treatment indicating phase crystallisation. As expected from binary phase diagrams (6–9), CeO_2, Co_3O_4, and CuO were the oxides formed as isolated phases.

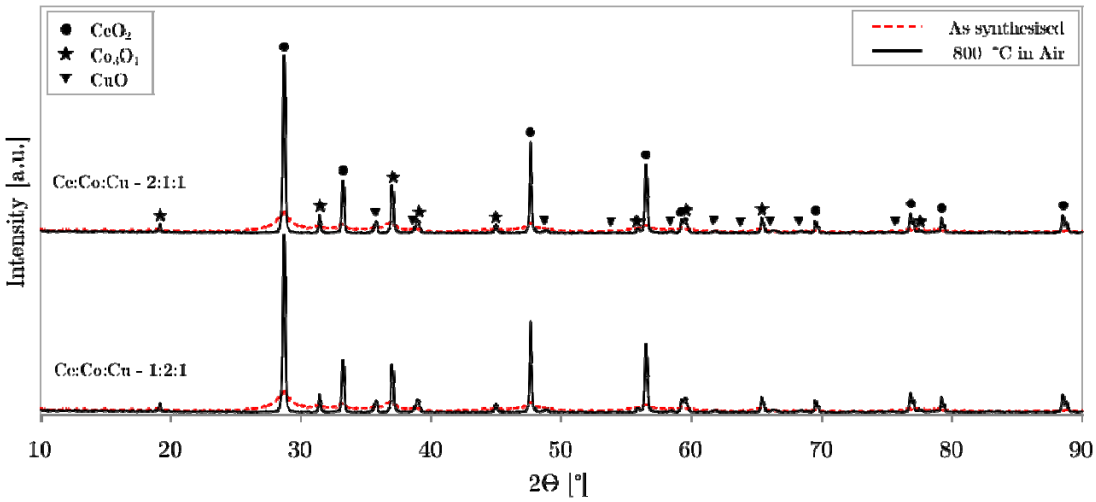

Figure 1. XRD spectra for the two compositions synthesised.

Rietveld refinement was performed over the raw data of the crystallised powders and the results are shown in Table I. The refinement was done considering PDF-03-065-2975, PDF-00-042-1467, and PDF-04-007-1375 for CeO_2, Co_3O_4, and CuO, respectively, as a starting point. From the PDF cards, CeO_2 has the cubic structure of fluorite with symmetry space group *Fm-3m*; Co_3O_4 is a cubic spinel with space group *Fd-3m*; and CuO has the monoclinic tenorite structure and space group *C 2/c*. Although the lattice parameters calculated slightly deviate from the theoretic values taken from PDF cards, it appears in the literature that Ce-Cu solid solutions are most likely not to occur (8).

However, cobalt has solubility in the ceria lattice (9), but no solid solution between these metals were found by X-ray analysis in this work.

TABLE I. Lattice parameters for the oxides - Rietveld refinement.

Composition	Oxide	a [Å]	b [Å]	c [Å]	α [°]	β [°]	γ [°]	Coeff.
Ce:Co:Cu - 2:1:1	CeO_2	5.4095	5.4095	5.4095	90.00	90.00	90.00	R_p= 27.8%
	Co_3O_4	8.0746	8.0746	8.0746	90.00	90.00	90.00	R_w= 15.6%
	CuO	4.6964	3.4080	5.1275	90.00	99.66	90.00	χ^2 = 1.14
Ce:Co:Cu - 1:2:1	CeO_2	5.4114	5.4114	5.4114	90.00	90.00	90.00	R_p= 33.3%
	Co_3O_4	8.0790	8.0790	8.0790	90.00	90.00	90.00	R_w= 16.9%
	CuO	4.6984	3.4105	5.1321	90.00	99.60	90.00	χ^2 = 1.04

The TPR profiles for both compositions are shown in Figure 2. Peak deconvolution was performed thus showing four peaks between 200 and 320˚C and two peaks at higher temperatures around 600−750˚C. The first four peaks most likely refer to the reduction steps of cobalt and copper oxides, according to Equations 5 to 8 (10).

$$Co_3O_4 + H_2 = 3CoO + H_2O \quad [5]$$

$$CoO + H_2 = Co + H_2O \quad [6]$$

$$2CuO + H_2 = Cu_2O + H_2O \quad [7]$$

$$Cu_2O + H_2 = 2Cu + H_2O \quad [8]$$

The last two peaks represent the reduction of ceria in two steps. The former is related to a ceria surface reduction whereas the latter represents bulk reduction (11).

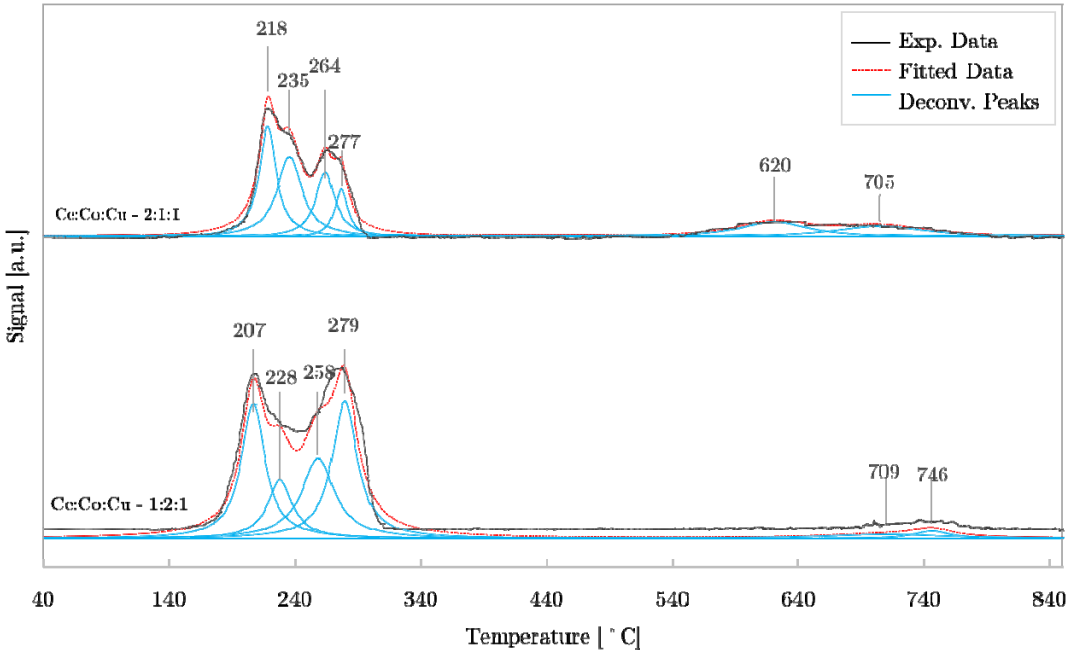

Figure 2. TPR profile for the two compositions analysed.

TPR results have shown the ability of the oxides to absorb hydrogen and be easily reduced into metals that may work properly as catalyst and as electrical percolated contact regarding cobalt and copper, respectively. Although cobalt and copper oxides are most likely to be reduced into metals, ceria will probably be reduced to CeO_{2-x} thus presenting lack of oxygen which polarises the structure and enhances conductivity.

The DC-conductivity results are shown in Figure 3. The activation energy (E_a) can be calculated from each slope of the two straight lines according to Equation 9:

$$\ln(\sigma) = \ln(\sigma_0) - E_a/(RT) \quad [9]$$

The activation energies calculated were 62.31 and 93.46 $kJmol^{-1}$ for Ce:Co:Cu – 2:1:1 and Ce:Co:Cu – 1:2:1 compositions, respectively. Although the conductivity of the cobalt-rich composition is slightly higher, it is also more temperature-dependant than the ceria-rich composition. It should be pointed out that the test was performed in an oxidising atmosphere aiming to measure the conductivity of the oxide mixture. Nevertheless, at operation conditions the compounds will be reduced and therefore, the conductivity under operating conditions will be increased.

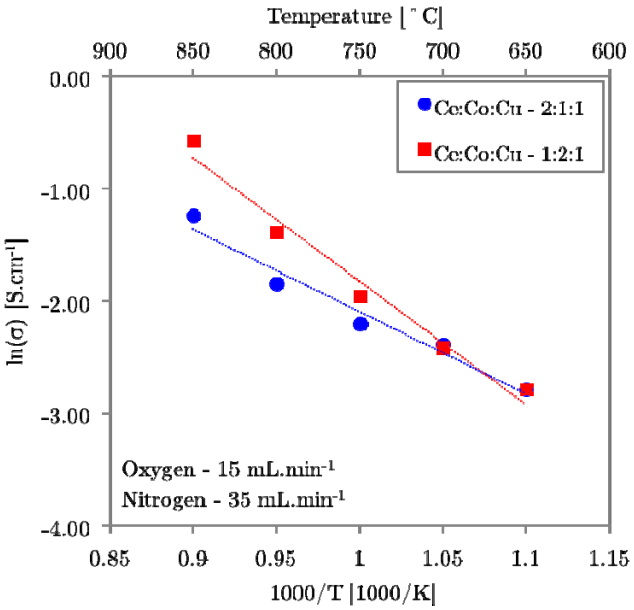

Figure 3. DC-Conductivity test for both oxides.

Figure 4 shows the maximum power density and open circuit voltage (OCV) for two cells fabricated (SOFC#1 and #2), and operated on hydrogen and methane fuels. The values have been compiled in Table II. It must be highlighted that these two sets of tests were performed with two cells in different test rigs at two different facilities. Therefore, the results have shown fair reproducibility for this material and the manufacturing procedures applied. Moreover, Figure 4e shows a result obtained with anhydrous ethanol as fuel using SOFC#1 that delivered over 150 $mWcm^{-2}$ of power density and an OCV of 1.02 V at 850˚C.

TABLE II: Results of i-V-curve testing of cells SOFC#1 and#2.

Cell	T [˚C]	Hydrogen fuel		Methane fuel	
		p_{mx} [mW cm^{-2}]	OCV [V]	p_{mx} [mW cm^{-2}]	OCV [V]

	750	127	1.12	10	1.01
SOFC#1	800	243	1.11	40	1.06
	850	383	1.09	88	1.09
	750	103	1.09		
SOFC#2	775			28	0.97
	800	160	1.08	60	1.03
	825			84	1.06
	850	265	1.07		

As could be seen, the cells have shown reasonable power densities with different fuels with no evident problem of gas tightness, as OCV values were as expected in all cases.

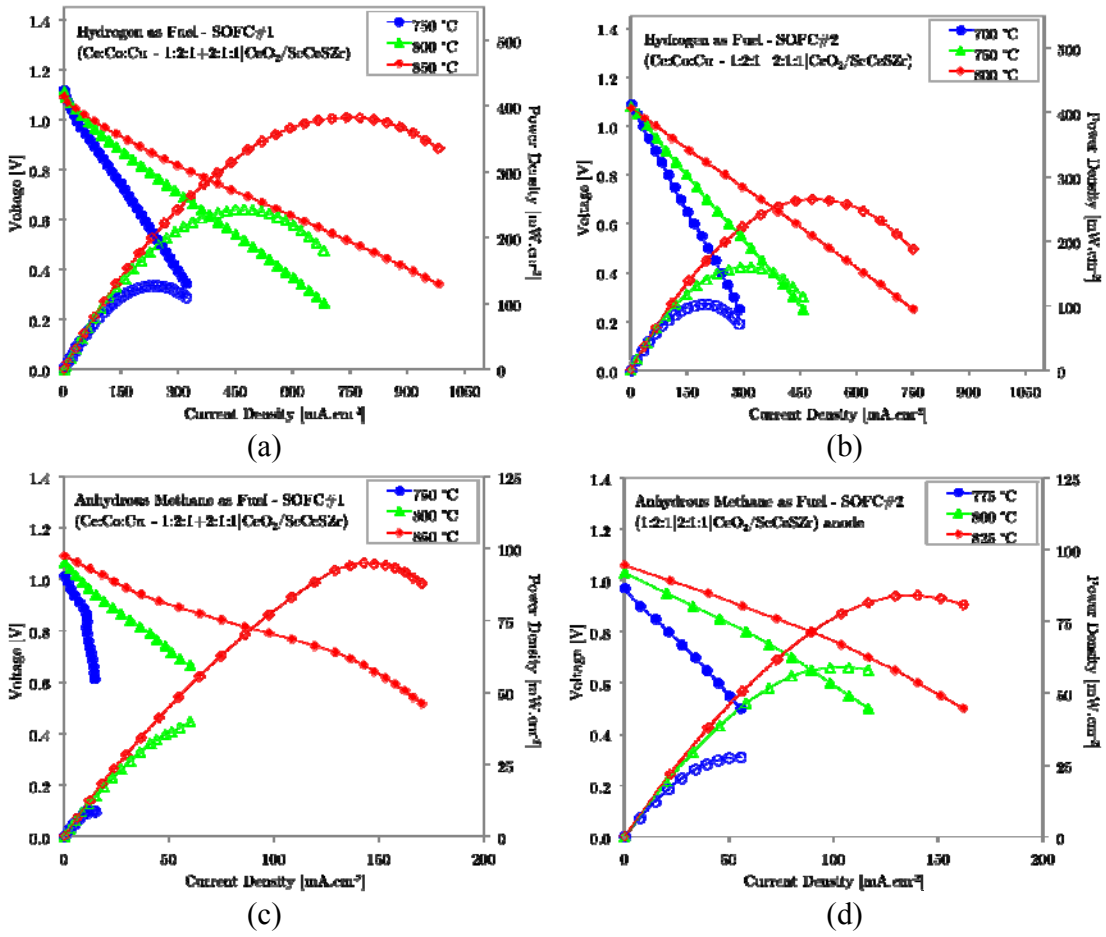

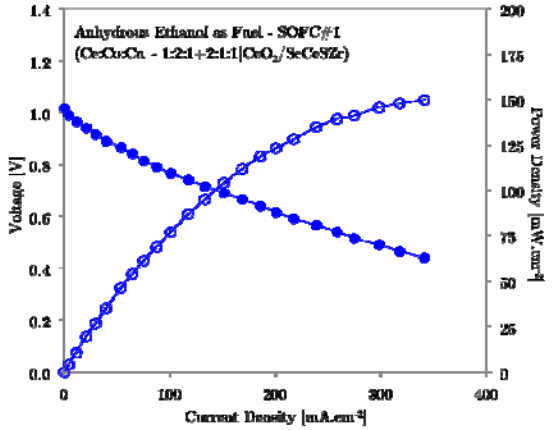

(e)

Figure 4. Electrochemical tests on two SOFC cells: with hydrogen fuel (a) SOFC#1, (b) SOFC#2, with methane (c) SOFC#1, (d) SOFC#2, and with ethanol (e) SOFC#1.

For the Raman spectrum shown in Figure 5 the peak spotted at 462 cm^{-1} refers to cerium oxide (12), whereas the peaks at 196 cm^{-1}, 482 cm^{-1}, 519 cm^{-1}, and 621 cm^{-1} are identified as cobalt oxide (13) and finally the peaks at 286 cm^{-1}, 347 cm^{-1}, and 550 cm^{-1} are copper oxides being the former and the second assigned to CuO and the latter as Cu_2O (13). The ceria peak at 462 cm^{-1} is assigned to CeF_{2g} due to the symmetrical stretching of the O-Ce-O vibrational unit in octahedral coordination (12).

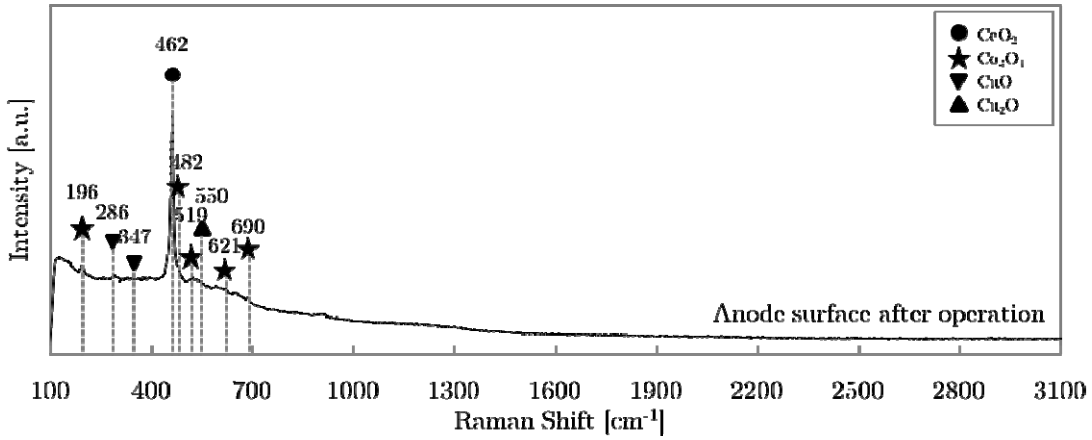

Figure 5. Raman spectrum of the anode surface after operation.

Cobalt oxide peaks are assigned respectively to E_g (482 cm^{-1}), F_{2g} (519 and 621 cm^{-1}) and A_{1g} (690 cm^{-1}) modes (13). Copper oxide presented modes A_g and B_g for 286 and 347 cm^{-1}, respectively (14).

The SEM images of the anode/electrolyte interface cross section are shown in Figure 6. The microstructure shows reasonable porosity and structural integrity after ageing for 50 hours in hydrogen-rich atmosphere. The cross section image gives an idea of layer thickness considering the inner layer (CeO_2-ScCeSZr) with a thickness around 6 µm whereas the subsequent anode layers (Ce:Co:Cu – 2:1:1 and Ce:Co:Cu – 1:2:1) have a thickness around 9 µm.

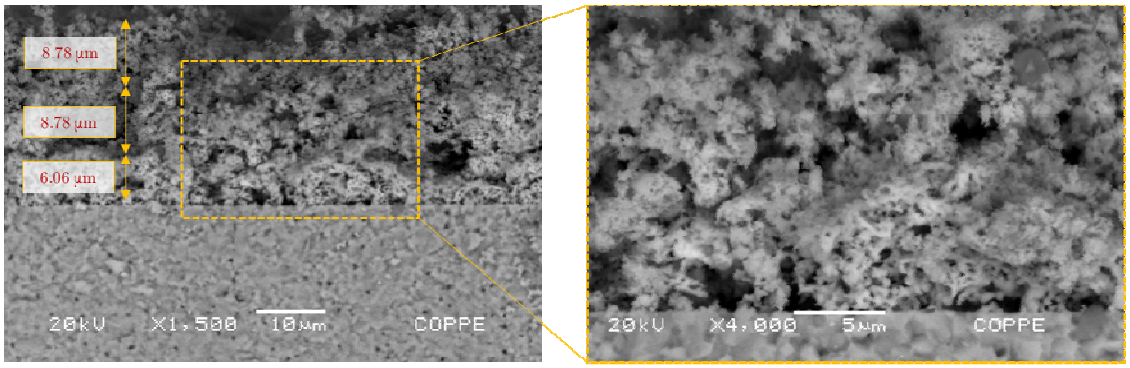

Figure 6. Scanning electron microscopy of the anode cross section.

The EDX images can be seen in Figure 7 including the information of zirconium, cerium, cobalt, and copper location, respectively. Using image analysis tools (*Metallographica* and *Matlab*), the EDX images were treated with low-pass filters such as a median filter aiming to eliminate noise, and then merged all together to reveal phase location, as can be seen in Figure 7f. Therefore, Figure 7f gives an idea of microstructure phase distribution as well as porosity and phase contiguity.

The double layered configuration of the anode was *a priori* designed to have a Cobalt-rich composition at the anode/gas interface that could promote internal reforming if needed, and a Cerium-rich composition near the electrolyte aiming to have a more suitable material for electrochemical oxidation. The inner layer was placed to increase anode/electrolyte adhesion and to eliminate any thermal incompatibility between metals and the electrolyte. The double layered anode configuration with inner layer was thus confirmed by SEM/EDX.

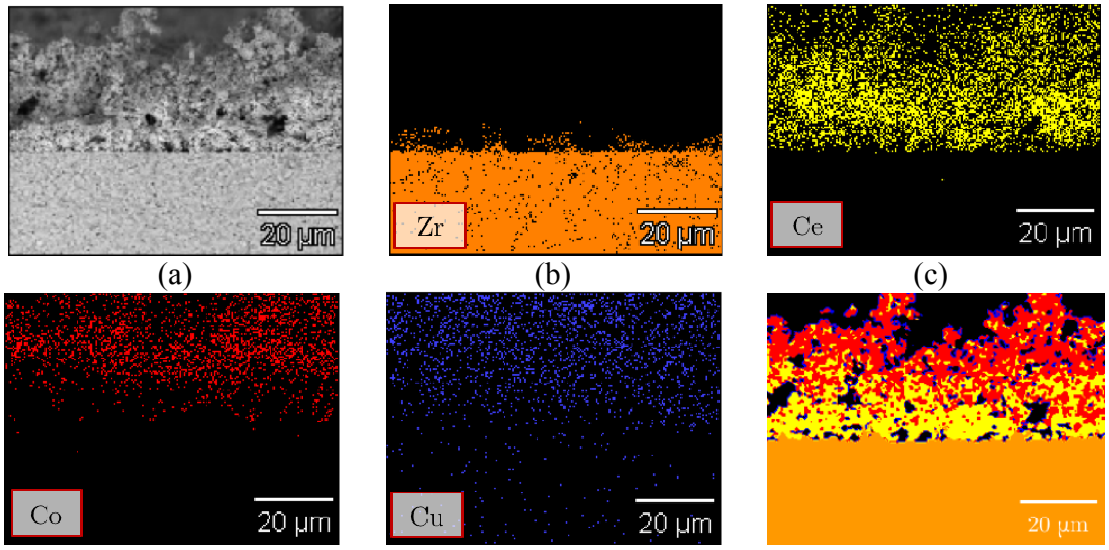

Figure 7. EDX mapping of the anode cross-section; (a) original image, (b) zirconium, (c) cerium, (d) cobalt, (e) copper, and (f) the merged images showing phase distribution.

Conclusions

The cerium-cobalt-copper material prepared has shown the ability of operating as SOFC anode with both pure methane and ethanol. In addition, manufacturing procedures and material synthesis have shown to be reproducible as different cells were tested in different test rig conditions with very similar results. The material synthesis proved to produce the oxide materials, as expected, in isolated phases. The bulk material has shown reasonable conductivity even in oxidising atmosphere, and TPR results proved the ability of oxides to reduce and to absorb hydrogen as expected from the literature. Finally, SEM/EDX showed that the microstructure presented enough porosity after ageing and phases were well distributed over the anode cross section.

Acknowledgments

The authors would like to acknowledge B.J.M.S's PhD scholarship, granted by the Brazilian National Council of Technological and Scientific Development (CNPq) and registered under the grant number 200665/2015-4. In addition, the financial support to this research from BNDES, Oxiteno S.A., and EnergiaH Ltda under grant number 11.2.0323 is gratefully acknowledged.

References

1. J. R. Rostrup-Nielsen, *Catal. Sci. Tech.*, **5**, 411 (1997).
2. J. Zhu, D. Zhang and K. D. King, *Fuel*, **80**, 899 (2001).
3. J. R. Rostrup-Nielsen J. B. Hansen and D. Helveg, *App. Phys. A.*, **85**, 427 (2006).
4. X.-F. Ye, S. R. Wang, Q. Hu *et al*, *Solid State Ion.*, **180**, 276 (2009).
5. S. A. Venancio, P. E. V. Miranda, *Cer. Intl.*, **37**, 3139 (2011).
6. T. Ivas, A. N. Grundy, E. Povoden-Karadeniz *et al*, *Calphad*, **36**, 57 (2012).
7. H. Okamoto, *ASM Alloy Phase Diagrams Center*, **2**, 1047 (2007).
8. W. Zhuang, Z. Y. Qiao, S. Wei, *J. Phase Equilibria*, **17**, 508 (1996).
9. T. Nishizawa, K. Ishida, *Bul. Alloy Phase Diagrams*, **5**, 161 (1984).
10. P. Arnoldy, J. A. Moulijn, *J. Catalysis*, **93**, 38 (1985).
11. J. Marrero-Jerez, A. Murugan, I. S. Metcalfe *et al*, *Cer. Intl.*, **40**, 15175 (2014).
12. B. M. Reddy, A. Khan, Y. Yamada, *et al.*, *J. Phys. Chem.*, **107**, 11475 (2003).
13. V. G. Hadjiev, M. N. Iliev and I. V. Vergilov, *J. Phys. C: S. State Phys.*, **21**, L199 (1988).
14. J. F. Xu, W. Ji, X. Shen, *et al.*, *J. Raman Spec.*, 30, **11** (1989).